Limnol. Oceanogr., 56(3), 2011, 1075–1092

doi:10.4319/lo.2011.56.3.1075

Sedimentary phosphorus dynamics and the evolution of bottom-water hypoxia: A coupled benthic–pelagic model of a coastal system

Daniel C. Reed,[a,*] Caroline P. Slomp,[a] and Bo G. Gustafsson[b]

[a] Department of Earth Sciences (Geochemistry), Faculty of Geosciences, Utrecht University, Utrecht, The Netherlands
[b] Baltic Nest Institute, Stockholm Resilience Centre, Stockholm University, Stockholm, Sweden

Abstract

The present study examines oxygen and phosphorus dynamics at a seasonally hypoxic site in the Arkona basin of the Baltic Sea. A coupled benthic–pelagic reactive-transport model is used to describe the evolution of bottom-water solute concentrations, as well as pore-water and sediment profiles. Aerobic respiration dominates remineralization, with iron reduction, denitrification, and sulphate reduction playing secondary roles, while other pathways are negligible. Sediments represent a significant oxygen sink chiefly due to the aerobic degradation of organic matter, as well as nitrification and iron oxyhydroxide precipitation. Most phosphorus deposited in sediments is in organic matter, yet cycling is dominated by iron-bound phosphorus due to rapid dissimilatory iron reduction coupled with aerobic iron oxyhydroxide formation. Sustained hypoxia results in an initial decrease in sediment phosphorus content due to dissolution of phosphorus-bearing iron oxyhydroxides, resulting in a pulse of phosphate to overlying waters. Although an organic-rich layer is formed under low-oxygen conditions, enhanced remineralization of organic phosphorus relative to organic carbon tempers sedimentary phosphorus accumulation. Upon reoxygenation of bottom waters after a decade of sustained hypoxia, oxygen concentrations do not immediately achieve values observed prior to hypoxia because the organic-rich layer creates a higher benthic oxygen demand. Artificial reoxygenation of bottom waters leads to a substantial increase in the iron-bound phosphorus pool; the total phosphorus content of the sediment, however, is unaffected. A relapse into hypoxia would consequently produce a large pulse of phosphate to the overlying waters potentially exacerbating the situation.

In recent times, hypoxic regions of the Baltic Sea (i.e., $[O_2] < 2$ mL L^{-1}) have grown to up to 60,000 km^2, largely in response to anthropogenic eutrophication (Savchuk et al. 2008; Conley et al. 2009a). The onset of hypoxia alters nutrient cycling (Vahtera et al. 2007) and is detrimental to benthic ecosystems, potentially reducing biodiversity due to mortality of species unable to tolerate low-oxygen or sulphidic conditions, thus altering community composition and function (Levin et al. 2009). Proliferation of nearshore hypoxia is associated with enhanced nutrient inputs due to human activities, such as agricultural use of fertilizers and sewage discharge. These extraneous nutrients stimulate primary productivity increasing the rain of organic material to underlying waters where it undergoes microbially mediated remineralization, consuming oxygen in the process. If ventilation of deeper waters by physical mixing is insufficient to balance oxygen demand, due to stratification or restrictive bathymetry, oxygen concentrations decline as a result.

Hypoxia and its associated problems are not unique to the Baltic Sea; such coastal dead zones have spread exponentially worldwide since the 1960s (Diaz and Rosenberg 2008). The deleterious effects and growing prominence of coastal hypoxia provide impetus for developing quantitative models of these systems to aid in the formulation of remediation strategies. In shallow coastal waters, sediments play an important role in the evolution of water-column chemistry because they regulate nutrient removal and recycling. By regenerating and reintroducing nutrients into the water column, sediments can help sustain enhanced primary production in overlying waters and potentially maintain bottom-water hypoxia. Phosphorus is an important nutrient in the Baltic Sea in this respect, because the change in the available dissolved inorganic phosphate has been shown to be positively correlated with the area of hypoxic bottom waters (Conley et al. 2002). Phosphorus cycling changes in response to the onset of hypoxia (Mortimer 1941; Ingall et al. 1993; Slomp et al. 2002), yet a comprehensive quantitative understanding of sedimentary phosphorus dynamics subject to transient redox conditions is lacking. Previous modeling studies of sediment biogeochemistry under oxygen-deficient waters, while insightful, either do not consider phosphorus cycling explicitly (Soetaert and Middelburg 2009) or do not account for potentially important feedbacks between sediments and overlying waters, such as the modulation of bottom-water solute concentrations (Katsev et al. 2007).

The present study examines the evolution of seasonal hypoxia at a site in the Arkona basin of the Baltic Sea. A coupled benthic–pelagic model is developed to study the biogeochemical response of sediments to changes in bottom-water redox conditions and the interplay between sediments and overlying waters. First, the model is ground-truthed using sediment and pore-water data for the Arkona Basin from Mort et al. (2010) and water-column data from the Baltic Environmental Database at Stockholm University. Then, simulations are undertaken to examine seasonal variations in organic-matter remineralization pathways, to establish the roles of oxygen-uptake mechanisms both in bottom waters and sediments, and to extricate the processes involved in sedimentary phosphorus cycling. Finally, we

* Corresponding author: d.reed@geo.uu.nl

Table 1. Chemical species included in the model.

Species	Notation	Type
Organic carbon*	$C_{org}^{\alpha,\beta,\gamma}$	Solid
Organic phosphorus*	$P_{org}^{\alpha,\beta,\gamma}$	Solid
Oxygen	O_2	Solute
Nitrate	NO_3^-	Solute
Manganese oxyhydroxides†	$MnO_2^{\alpha,\beta}$	Solid
Iron oxyhydroxides†	$Fe(OH)_3^{\alpha,\beta}$	Solid
Sulphate	$SO_4^=$	Solute
Manganese	Mn^{2+}	Solute
Iron	Fe^{2+}	Solute
Ammonia and ammonium‡	ΣNH_4^+	Solute
Phosphate§	$\Sigma H_2PO_4^-$	Solute
Hydrogen sulphide‖	ΣH_2S	Solute
Methane	CH_4	Solute
Elemental sulphur	S_0	Solid
Iron monosulphide	FeS	Solid
Pyrite	FeS_2	Solid
Iron-bound phosphate†	$Fe–P^{\alpha,\beta}$	Adsorbed and co-precipitated
Authigenic phosphate	Auth–P	Solid

* There are three pools of organic species: (α) rapidly oxidized, (β) slowly oxidized, and (γ) refractory.
† There are two forms of Mn- and Fe-oxyhydroxides: (α) amorphous, and (β) more crystalline.
‡ $\Sigma NH_4^+ = NH_4^+ + NH_3$.
§ $\Sigma H_2PO_4^- = H_3PO_4 + H_2PO_4^- + HPO_4^= + PO_4^{3-}$.
‖ $\Sigma H_2S = H_2S + HS^- + S^=$.

use the model to investigate the implications of expanding hypoxia in the Baltic Sea by simulating a decline in water-column mixing and examining how the system responds to the resulting hypoxia and recovers when stagnation subsides or bottom waters are artificially reoxygenated.

Methods

Coupled benthic–pelagic biogeochemical model—Sediment biogeochemistry is influenced by the chemistry of overlying waters, which is, in turn, influenced by sediment biogeochemistry. Although diagenetic models alone provide insight into the response of sedimentary geochemistry to transient redox conditions (Katsev et al. 2006, 2007; Morse and Eldridge 2007), a coupled benthic–pelagic model provides a more realistic description by allowing feedback between sediments and the water column (Soetaert and Middelburg 2009). Rather than having to *prescribe* temporally variable boundary conditions at the sediment–water interface, a coupled model allows bottom-water conditions to evolve naturally, furnishing insight into benthic–pelagic interactions. Boundary conditions must be prescribed for surface waters; however, these parameters are often better constrained due to more extensive sampling. For these reasons, the model used in the present study comprises a multicomponent diagenetic module (Boudreau 1996; Soetaert et al. 1996; Wang and Van Cappellen 1996) coupled to a simple two-layer water column (i.e., surface and deep waters).

Within the diagenetic component, a system of partial differential equations describes the mass balance of 25 chemical species (Table 1), which are subject to physical and biological transport, as well as a suite of reactions (Table 2). Solids and solutes are transported by bioturbation and buried as material accumulates at the sediment–water interface. Dissolved species are also subject to molecular diffusion. The generic mass conservation equations for solids and solutes in sediments are, respectively,

$$\frac{\partial C_s}{\partial t} = \frac{1}{\phi_s}\frac{\partial}{\partial x}\left(\phi_s D_b \frac{\partial C_s}{\partial x} - \phi_s u C_s\right) + \sum \mathrm{R}_s \quad (1)$$

$$\frac{\partial C_p}{\partial t} = \frac{1}{\phi}\frac{\partial}{\partial x}\left[\phi\left(\frac{D'}{\theta^2} + D_b\right)\frac{\partial C_p}{\partial x} - \phi v C_p\right] + \sum \mathrm{R}_p \quad (2)$$

where C_p is concentration of a solute in mass per unit volume of pore water (μmol L^{-1}), C_s is concentration of a particulate species in mass per unit volume of solids (μmol L^{-1}), t is time (yr), x is distance from the sediment–water interface (cm), ΣR_s is the net reaction rate per unit volume of solids (μmol L^{-1} yr^{-1}), ΣR_p is the net reaction rate per unit volume of pore water (μmol L^{-1} yr^{-1}), D_b is the biodiffusion coefficient (cm^2 yr^{-1}), D' is the appropriate molecular diffusion coefficient adjusted for viscosity and temperature (cm^2 yr^{-1}), u is the burial velocity of solids (cm yr^{-1}), v is the burial velocity of pore water (cm yr^{-1}), ϕ is porosity (cm^3 cm^{-3}), ϕ_s is the solid volume fraction ($\phi_s = 1 - \phi$; cm^3 cm^{-3}), and θ^2 is tortuosity (unitless) (Boudreau 1997).

Bioturbation is modeled as a diffusive process, termed *biodiffusion* (D_b), representing random small-scale displacements of particles and pore water by benthic fauna (Goldberg and Koide 1962; Guinasso and Schink 1975; Boudreau 1986). The intensity of biogenic mixing is assumed to decrease exponentially with depth to account for the decline in faunal density with increasing depth into the sediment (Boudreau 1986). Bioturbation is, thus, defined in the model domain by two parameters: x_b, the

Table 2. Chemical reactions included in the model.

Primary redox reactions*

$$OM + aO_2 \rightarrow aCO_2 + bNH_4^+ + cH_3PO_4 + aH_2O \quad (R1)$$

$$OM + \tfrac{4a}{5}NO_3^- + \tfrac{4a}{5}H^+ \rightarrow aCO_2 + bNH_4^+ + cH_3PO_4 + \tfrac{2a}{5}N_2 + \tfrac{7a}{5}H_2O \quad (R2)$$

$$OM + 2aMnO_2^{\alpha} + 4aH^+ \rightarrow aCO_2 + bNH_4^+ + cH_3PO_4 + 2aMn^{2+} + 3aH_2O \quad (R3)$$

$$OM + 4aFe(OH)_3^{\alpha} + 4a\chi Fe - P^{\alpha} + 12aH^+ \rightarrow aCO_2 + bNH_4^+ + (c + 4a\chi)H_3PO_4 + 4aFe^{2+} + 13aH_2O \quad (R4)$$

$$OM + \tfrac{a}{2}SO_4^{=} + aH^+ \rightarrow aCO_2 + bNH_4^+ + cH_3PO_4 + \tfrac{a}{2}H_2S + aH_2O \quad (R5)$$

$$OM \rightarrow \tfrac{a}{2}CO_2 + bNH_4^+ + cH_3PO_4 + \tfrac{a}{2}CH_4 \quad (R6)$$

Other reactions†

$$2O_2 + NH_4^+ + 2HCO_3^- \rightarrow NO_3^- + 2CO_2 + 3H_2O‡ \quad (R7)$$

$$O_2 + 2Mn^{2+} + 4HCO_3^- \rightarrow 2MnO_2^{\alpha} + 4CO_2 + 2H_2O‡ \quad (R8)$$

$$O_2 + 4Fe^{2+} + 8HCO_3^- + H_2O + 4\chi H_2PO_4^- \rightarrow 4Fe(OH)_3^{\alpha} + 4\chi Fe - P^{\alpha} + 8CO_2‡ \quad (R9)$$

$$2O_2 + FeS \rightarrow SO_4^{=} + Fe^{2+} \quad (R10)$$

$$7O_2 + 2FeS_2 + 2H_2O \rightarrow 4SO_4^{=} + 2Fe^{2+} + 4H^+ \quad (R11)$$

$$2O_2 + H_2S + 2HCO_3^- \rightarrow SO_4^{=} + 2CO_2 + 2H_2O‡ \quad (R12)$$

$$O_2 + CH_4 \rightarrow CO_2 + H_2O‡ \quad (R13)$$

$$MnO_2^{\alpha,\beta} + 2Fe^{2+} + 2\chi H_2PO_4^- + 2H_2O + 2HCO_3^- \rightarrow 2Fe(OH)_3^{\alpha} + 2\chi Fe - P^{\alpha} + Mn^{2+} + 2CO_2 \quad (R14)$$

$$MnO_2^{\alpha,\beta} + H_2S + 2CO_2 \rightarrow Mn^{2+} + S_0 + 2HCO_3^- \quad (R15)$$

$$2Fe(OH)_3^{\alpha,\beta} + 2\chi Fe - P^{\alpha,\beta} + H_2S + 4CO_2 \rightarrow 2Fe^{2+} + 2\chi H_2PO_4^- + S_0 + 4HCO_3^- + 2H_2O \quad (R16)$$

$$Fe^{2+} + H_2S \rightarrow FeS + 2H^+‡ \quad (R17)$$

$$SO_4^{=} + CH_4 + CO_2 \rightarrow 2HCO_3^- + H_2S‡ \quad (R18)$$

$$4S_0 + 4H_2O \rightarrow 3H_2S + SO_4^{=} + 2H^+ \quad (R19)$$

$$FeS + S_0 \rightarrow FeS_2 \quad (R20)$$

$$Fe(OH)_3^{\alpha} + \chi Fe - P^{\alpha} \rightarrow Fe(OH)_3^{\beta} + \chi Fe - P^{\beta} \quad (R21)$$

$$MnO_2^{\alpha} \rightarrow MnO_2^{\beta} \quad (R22)$$

* Organic matter (OM) is of the form $(CH_2O)_a(NH_4^+)_b(H_3PO_4)_c$.
† χ denotes the ratio of adsorbed or co-precipitated phosphorus with iron oxyhydroxides.
‡ Indicates reactions that also occur in the deep-water layer.

characteristic mixing depth of the benthic community (cm), and D_{b0}, the mixing intensity at the sediment–water interface ($cm^2\ yr^{-1}$). Bioirrigation is omitted from Eq. 2, because it appears to be of negligible importance at our study site. This is discussed in detail in the Model application section. Deposition of material at the sediment surface leads to a downward advective flux of all species, because the origin of the model's reference frame is tied to the sediment–water interface. During burial, sediment undergoes compaction, leading to spatially variable porosity and depth-dependent burial velocities for both particulate material and pore water. The model assumes porosity (ϕ) decreases exponentially from a value of ϕ_0 at the sediment–water to an asymptote at depth, ϕ_∞ (Table 3). These parameters are estimated by fitting the porosity function to an observed profile, which is assumed to be temporally invariable implying steady-state compaction. Molecular diffusion is impeded by the presence of particles; tortuosity scales the diffusion coefficient to account for this (Table 3). Molecular diffusion coefficients are taken from Van Cappellen and Wang (1995) and adjusted according to the formulas presented within that paper. The suite of reactions included in the model is composed of reactions taken from Boudreau (1996), Wang and Van Cappellen (1996), and Berg et al. (2003; Table 2). Rate constants for these reactions are for the most part taken from the literature; their sources are given in Table 4. Details of the equations used to describe reaction kinetics are provided as Tables 5 and 6.

The diagenetic module interfaces with the water column by means of a homogeneous deep-water layer overlying the sediment. Solutes within the layer are exchanged with adjacent waters through physical mixing and with sediments through diffusive fluxes. Furthermore, at the uppermost grid point in the sediment solutes may be directly added to or removed from the water column by means of interfacial reactions, that is, diagenetic reactions occurring at the sediment–water interface. Only dissolved species are present within the bottom waters and interact with one-another through a reduced set of the reactions prescribed within the sediments (reactions R7, R8, R9, R12, R13, R17, and R18; Table 2); and any particulate material precipitated by these reactions (i.e., Mn- and Fe-oxyhydroxides) is immediately deposited at the sediment–water interface. The mass balance of the components present in the bottom water is described by a system of ordinary differential equations. Within these equations, the rate of change of solute concentrations due to water-column exchange is calculated as the difference in source and deep concentrations multiplied by an exchange coefficient, η (yr^{-1}), while diffusive exchange across the sediment–water interface is modeled using eq. 5.43 of Boudreau (1997) as shown in the equation below (second term of the right-hand side).

Table 3. Environmental and transport parameters.

Parameter	Value or expression	Units	Source
Porosity	$\phi(x)=\phi_\infty+(\phi_0-\phi_\infty)\exp\left(-\frac{x}{\lambda}\right)$	$cm^3\ cm^{-3}$	a
Porosity at surface	$\phi_0=0.943$	$cm^3\ cm^{-3}$	b
Porosity at depth	$\phi_\infty=0.877$	$cm^3\ cm^{-3}$	b
Porosity e-folding distance	$\lambda=5.301$	cm	b
Solid volume fraction	$\phi_s(x)=1-\phi$	$cm^3\ cm^{-3}$	b
Tortuosity	$\theta^2(\phi)=1-2\ \ln\phi$	—	a
Sediment density	$\rho_s=2.65$	$g\ cm^{-3}$	—
Accumulation rate	$F_{sed}=0.122$	$g\ cm^{-2}\ yr^{-1}$	b
Height of bottom-water layer	$H=5$	m	c
Biodiffusion	$D_b(x)=D_{b0}\ \exp\left(-\frac{x}{x_b}\right)$	$cm^2\ yr^{-1}$	—
Biodiffusion coefficient at surface	$D_{b0}(T)=5.411\left(\frac{T}{T_{max}}\right)$	$cm^2\ yr^{-1}$	c
Mixed-layer depth	$x_b([O_2])=\begin{cases}10\times\left(\frac{[O_2]}{[O_2]_{source}}\right) & [O_2]_{source}\geq[O_2]\geq 0\\ 10 & [O_2]>[O_2]_{source}\end{cases}$	cm	—
P : Fe ratio for iron-bound phosphorus	$\chi=0.175$	—	b
Refractory $Fe(OH)_3$ in sediment	1	$\mu mol\ g^{-1}$	b
Refractory MnO_2 in sediment	0.2	$\mu mol\ g^{-1}$	b
Refractory S in sediment	0.15	$mmol\ g^{-1}$	b

a) Boudreau (1997).
b) Mort et al. (2010).
c) Model constrained.

The general mass conservation equation for bottom-water solutes is

$$\frac{dC_{bw}}{dt}=\eta\left(C_{adj}-C_{bw}\right)+\frac{D'}{\theta^2}\frac{\phi}{H}\left.\frac{\partial C_p}{\partial x}\right|_0+\sum R_{bw} \qquad (3)$$

where C_{bw} is the concentration of a solute in the deep waters in mass per unit volume of water ($\mu mol\ L^{-1}$), C_{adj} is the concentration of a solute in the adjacent waters in mass per unit volume of water ($\mu mol\ L^{-1}$), H is the height of the deep layer (cm), $\left.\frac{\partial C_p}{\partial x}\right|_0$ is the gradient of the solute profile at the sediment–water interface ($\mu mol\ L^{-1}\ cm^{-1}$), ΣR_{bw} is the net reaction rate per unit volume of water ($\mu mol\ L^{-1}\ yr^{-1}$), and all other symbols retain their previous definitions. The behavior within the source waters is prescribed not calculated, so no mass balance equations are required.

Organic-matter dynamics—Organic-matter decomposition drives the geochemistry of marine sediments. The order in which oxidants are used in the remineralization of organics depends on the free-energy yield of the reaction (Froelich et al. 1979). Here, the succession of oxidants is described by means of a Monod scheme (Table 5), whereby those oxidants with the highest energy yield are used preferentially until they become limiting and the oxidant with the next highest energy yield is used (Boudreau 1997). Oxidants considered by the model are oxygen, nitrate, manganese oxides, iron oxides, and sulphate. Following exhaustion of these species as terminal electron acceptors, organic-matter remineralization occurs by methanogenesis.

Because organic matter is composed of constituents that degrade at different rates (e.g., lignins vs. proteins), a 'multi-G' approach is used to describe organic-matter degradation that allows organic matter to be divided into pools with different reactivities (Jørgensen 1978; Westrich and Berner 1984). In our model, three pools of organic matter are used: highly reactive, less reactive, and nonreactive. Rate constants for the reactive components are determined using empirical relationships from Tromp et al. (1995). These rate constants are attenuated by a multiplication factor Ψ for sulphate reduction and methanogenesis to account for slower remineralization via these pathways (Moodley et al. 2005). To use a multi-G approach, the depositional flux of organic matter in the model must be divided into its constituent types. Westrich and Berner (1984) determined that fresh planktonic material is 50% highly reactive, 16% less reactive, and 34% nonreactive organic matter and calculated the first-order rate constants for the decay of the highly and less reactive pools as 24 ± 4 yr^{-1} and 1.4 ± 0.7 yr^{-1}, respectively. Organic matter is assumed to decompose for 3 weeks before being deposited at the sediment–water interface.

Accelerated organic phosphorus remineralization—Under sustained hypoxia, organic phosphorus is remineralized preferentially to organic carbon (Ingall et al. 1993; Ingall and Jahnke 1994; Slomp et al. 2002). Normally, phosphorus remineralization is calculated in the model by multiplying the remineralization rate of organic carbon by [P_{org}/C_{org}] for the considered organic pool. To simulate enhanced phosphorus regeneration, we assume phosphorus remineralization is accelerated by a factor ε, which is constant in time and space. Stated mathematically,

$$R^{\alpha}_{P_{org}}=\varepsilon R^{\alpha}_{C_{org}}\left(\frac{\left[P^{\alpha}_{org}\right]}{\left[C^{\alpha}_{org}\right]}\right) \qquad (4)$$

where $R^{\alpha}_{P_{org}}$ is the remineralization rate of labile organic phosphorus, $R^{\alpha}_{C_{org}}$ is the remineralization rate of labile

Table 4. Reaction parameters. Limiting concentrations double as inhibition coefficients in the Monod scheme (Boudreau 1996).

Parameter	Symbol	Value	Units	Source	Range given by source (values used by source)
Decay constant for organic matter type α	k_α	1.62	yr^{-1}	a	Empirical model
Decay constant for organic matter type β	k_β	0.0086	yr^{-1}	a	Empirical model
Limiting concentration of O_2	k_{O_2}	20	$\mu mol\ L^{-1}$	b	1–30, (20)
Limiting concentration of NO_3^-	$k_{NO_3^-}$	4	$\mu mol\ L^{-1}$	b	4–80, (2)
Limiting concentration of MnO_2	k_{MnO_2}	4	$\mu mol\ g^{-1}$	b	4–32, (4, 16, 32)
Limiting concentration of $Fe(OH)_3$	$k_{Fe(OH)_3}$	65	$\mu mol\ g^{-1}$	b	65–100, (65, 100)
Limiting concentration of $SO_4^=$	$k_{SO_4^=}$	1.6	$mmol\ L^{-1}$	b	1.6, (1.6)
Attenuation factor for $SO_4^=$ reduction	Ψ	0.075	—	—	—
Rate constant for reaction E7	k_1	10,000	$mmol^{-1}\ L\ yr^{-1}$	b	≈10,000, (5000)
Rate constant for reaction E8	k_2	20,000	$mmol^{-1}\ L\ yr^{-1}$	b	800–20,000, (5000,10,000)
Rate constant for reaction E9	k_3	140,000	$mmol^{-1}\ L\ yr^{-1}$	b	140,000, (140,000)
Rate constant for reaction E10	k_4	300	$mmol^{-1}\ L\ yr^{-1}$	b	300, (300)
Rate constant for reaction E11	k_5	1	$mmol^{-1}\ L\ yr^{-1}$	b	1
Rate constant for reaction E12	k_6	160	$mmol^{-1}\ L\ yr^{-1}$	b	≥160, (160)
Rate constant for reaction E13	k_7	10,000,000	$mmol^{-1}\ L\ yr^{-1}$	b	10,000,000, (10,000,000)
Rate constant for reaction E14	k_8	2	$mmol^{-1}\ L\ yr^{-1}$	c	2, (2)
Rate constant for reaction E15	k_9	20	$mmol^{-1}\ L\ yr^{-1}$	b	≤100,000, (20)
Rate constant for reaction E16	k_{10}	8	$mmol^{-1}\ L\ yr^{-1}$	b	≤100, (8)
Rate constant for reaction E17	k_{11}	100	$mmol^{-1}\ L\ yr^{-1}$	c	14,822, (14,822)
Rate constant for reaction E18	k_{12}	10	$mmol^{-1}\ L\ yr^{-1}$	b	≈10, (10)
Rate constant for reaction E19	k_{13}	3	yr^{-1}	c	3, (3)
Rate constant for reaction E20	k_{14}	7	$mmol^{-1}\ L\ yr^{-1}$	c	7, (7)
Rate constant for reaction E21	k_{15}	0.6	yr^{-1}	c	0.6, (0.6)
Rate constant for reaction E22	k_{16}	1.8	yr^{-1}	c	1.8, (1.8)

a) Tromp et al. (1995).
b) Wang and Van Cappellen (1996).
c) Berg et al. (2003).

organic carbon, and P_{org}^{α} and C_{org}^{α} are the concentrations of labile organic phosphorus and carbon, respectively. Under oxic conditions, ε is equal to 1; a value > 1 corresponds to accelerated organic phosphorus remineralization.

Iron and manganese oxyhydroxides—Like organic matter, iron and manganese oxyhydroxides are divided into pools based on reactivity. There are two reactive pools representing amorphous and well-crystalline species; both are reduced through reaction with hydrogen sulphide (R16), while the former is also available for dissimilatory reduction (R4). As oxyhydroxides age, they are transformed from amorphous to well-crystalline according to first-order kinetics. Using a similar multicomponent diagenetic model, Berg et al. (2003) estimated the rate constants for the transformation of manganese and iron oxyhydroxides as 1.8 yr^{-1} and 0.6 yr^{-1}, respectively. In the present study, we use these same rate constants. In addition, an inert background concentration is assumed throughout the domain to allow for the presence of unreactive material at depth (Table 3).

Model solution—The model outlined above is solved numerically using the Method of Lines approach. Spatial derivatives within the partial differential equations are replaced by finite difference approximations resulting in a system of ordinary differential equations (ODEs), which are then integrated numerically using the Variable Coefficient Ordinary Differential Equations (VODE) solver (Soetaert et al. 2010). The finite differencing method used is the blended scheme published by Fiadeiro and Veronis (1977). An even grid spacing with 271 nodes (i.e., 1-mm resolution) is employed and achieves good mass balance. The model definition is written in C and compiled into a library for use with the software package R (R Development Core Team 2006; Soetaert and Herman 2009). An R script specifies the initial conditions, boundary conditions, parameter values, and other details of the simulation and passes these values, as well as the compiled model definition, to the ODE solver. VODE then provides the model solution at requested times throughout the model run.

Model application—The model was applied to a site in the Arkona basin of the Baltic Sea. The Arkona basin is roughly 19,000 km^2 in area with a maximum depth of 53 m (Zettler et al. 2006) and is located between Bornholm and the Danish Straits. The field station considered, BY2 (54°58.504N 14°05.937E), is situated in the deeper region of the basin at a water depth of 47 m. Mean monthly bottom-water temperatures vary between 3.3°C and 13.7°C throughout the year (Fig. 1). The average salinity of bottom waters is ~ 14 and 8 for surface waters; the water column exhibits strong stratification throughout the year (Gustafsson 2001).

Table 5. Primary redox reaction equations. These equations are used to divide decomposition of organics between oxidants, according to their availability and energy yield. For example, $R^i_{O_2}$ gives the decomposition rate of organic type i (*see* text) due to aerobic respiration.

$$R^i_{O_2} = k_i C^i_{org}\left(\frac{[O_2]}{k_{O_2}+[O_2]}\right) \quad \text{(E1)}$$

$$R^i_{NO_3^-} = k_i C^i_{org}\left(\frac{[NO_3^-]}{k_{NO_3^-}+[NO_3^-]}\right)\left(\frac{k_{O_2}}{k_{O_2}+[O_2]}\right) \quad \text{(E2)}$$

$$R^i_{MnO_2} = k_i C^i_{org}\left(\frac{[MnO_2]}{k_{MnO_2}+[MnO_2]}\right)\left(\frac{k_{NO_3^-}}{k_{NO_3^-}+[NO_3^-]}\right)\left(\frac{k_{O_2}}{k_{O_2}+[O_2]}\right) \quad \text{(E3)}$$

$$R^i_{Fe(OH)_3} = k_i C^i_{org}\left(\frac{[Fe(OH)_3]}{k_{Fe(OH)_3}+[Fe(OH)_3]}\right)\left(\frac{k_{MnO_2}}{k_{MnO_2}+[MnO_2]}\right)\left(\frac{k_{NO_3^-}}{k_{NO_3^-}+[NO_3^-]}\right)\left(\frac{k_{O_2}}{k_{O_2}+[O_2]}\right) \quad \text{(E4)}$$

$$R^i_{SO_4^=} = \Psi k_i C^i_{org}\left(\frac{[SO_4^=]}{k_{SO_4^=}+[SO_4^=]}\right)\left(\frac{k_{Fe(OH)_3}}{k_{Fe(OH)_3}+[Fe(OH)_3]}\right)\left(\frac{k_{MnO_2}}{k_{MnO_2}+[MnO_2]}\right)\left(\frac{k_{NO_3^-}}{k_{NO_3^-}+[NO_3^-]}\right)\left(\frac{k_{O_2}}{k_{O_2}+[O_2]}\right) \quad \text{(E5)}$$

$$R^i_{CH_4} = \Psi k_i C^i_{org}\left(\frac{k_{SO_4^=}}{k_{SO_4^=}+[SO_4^=]}\right)\left(\frac{k_{Fe(OH)_3}}{k_{Fe(OH)_3}+[Fe(OH)_3]}\right)\left(\frac{k_{MnO_2}}{k_{MnO_2}+[MnO_2]}\right)\left(\frac{k_{NO_3^-}}{k_{NO_3^-}+[NO_3^-]}\right)\left(\frac{k_{O_2}}{k_{O_2}+[O_2]}\right) \quad \text{(E6)}$$

The benthic biomass of the deep Arkona basin is dominated by bivalves, specifically *Macoma balthica* (Zettler et al. 2006). *M. balthica* does not construct and ventilate burrows like tube-dwelling worms, but is capable of enhancing solute transport by virtue of its feeding strategy. Particles and water are drawn into an inhalant siphon at or above the sediment–water interface and expelled from an exhalant siphon usually within the sediment column (Reise 1983). Yet despite this potential bioirrigation mechanism, no appreciable effects are apparent from the available sediment and pore-water data.

Bioirrigation has the potential to significantly alter the redox conditions of sediments and depth distribution of solutes, such as ammonium and dissolved silica (Boudreau and Marenelli 1994). Nevertheless, there is no evidence of bioirrigation in either the ammonium profile (Fig. 2) or the silica profile (data not shown). Particulate species are also affected by enhanced solute exchange with overlying waters. Simulations undertaken with the model in which bioirrigation was included as a nonlocal reaction term (Boudreau 1984; Emerson et al. 1984) demonstrate that iron oxyhydroxides persist for longer when bioirrigators are present due to enhanced oxygenation of surficial sediment. As a result, they are able to crystallize into forms unavailable for dissimilatory iron reduction (*see* reaction R21) and are, thus, retained within the sediment for longer. Consequently, the modeled iron oxyhydroxide, dissolved iron, and phosphate profiles differ markedly from observation when bioirrigation occurs at a nonnegligible rate: iron oxyhydroxides are overestimated at depth, while the peaks in phosphate and dissolved iron near the sediment–water interface are underestimated. Thus, although *M. balthica* has the *potential* to enhance solute exchange between the sediment and water column, geochemical data suggest that these effects are unimportant at BY2. This is likely due to their physiology and vertical distribution in the sediment column. The exhalant siphon of *M. balthica* is typically shorter than the inhalant siphon and, therefore, water and faeces are expelled within the sediment column (Reise 1983). Low oxygen conditions, however, cause *M. balthica* to migrate toward the sediment surface (Long et al. 2008) and discharge waste material in the vicinity of the sediment–water interface. Indeed, *M. balthica* has often been observed with their exhalant siphon flush to the sediment surface in this manner (Gilbert 1977). As a result, there is no net transfer of oxygenated water across the sediment–water interface explaining why bioirrigation is of negligible importance at BY2.

Table 6. Secondary redox and other reaction equations.

$R_1 = k_1[O_2][\Sigma NH_4^+]$	(E7)
$R_2 = k_2[O_2][Mn^{2+}]$	(E8)
$R_3 = k_3[O_2][Fe^{2+}]$	(E9)
$R_4 = k_4[O_2][FeS]$	(E10)
$R_5 = k_5[O_2][FeS_2]$	(E11)
$R_6 = k_6[O_2][\Sigma H_2S]$	(E12)
$R_7 = k_7[O_2][CH_4]$	(E13)
$R_8 = k_8[MnO_2^{\alpha,\beta}][Fe^{2+}]$	(E14)
$R_9 = k_9[MnO_2^{\alpha,\beta}][\Sigma H_2S]$	(E15)
$R_{10} = k_{10}[Fe(OH)_3^{\alpha,\beta}][\Sigma H_2S]$	(E16)
$R_{11} = k_{11}[Fe^{2+}][\Sigma H_2S]$	(E17)
$R_{12} = k_{12}[SO_4^=][CH_4]$	(E18)
$R_{13} = k_{13}[S_0]$	(E19)
$R_{14} = k_{14}[FeS][S_0]$	(E20)
$R_{15} = k_{15}[Fe(OH)_3^{\alpha}]$	(E21)
$R_{16} = k_{16}[MnO_2^{\alpha}]$	(E22)

Field data with which to compare the model were taken from the Baltic Environmental Database at Stockholm University for annual bottom-water time series and from Mort et al. (2010) for sediment and pore-water profiles, sampled September 2007. This setting was chosen because it allows the effects of transient redox conditions on biogeochemical processes to be explored (*see* Fig. 1b). At the time of sampling, bottom waters were hypoxic (Mort et al. 2010). All analysis techniques and sampling methods

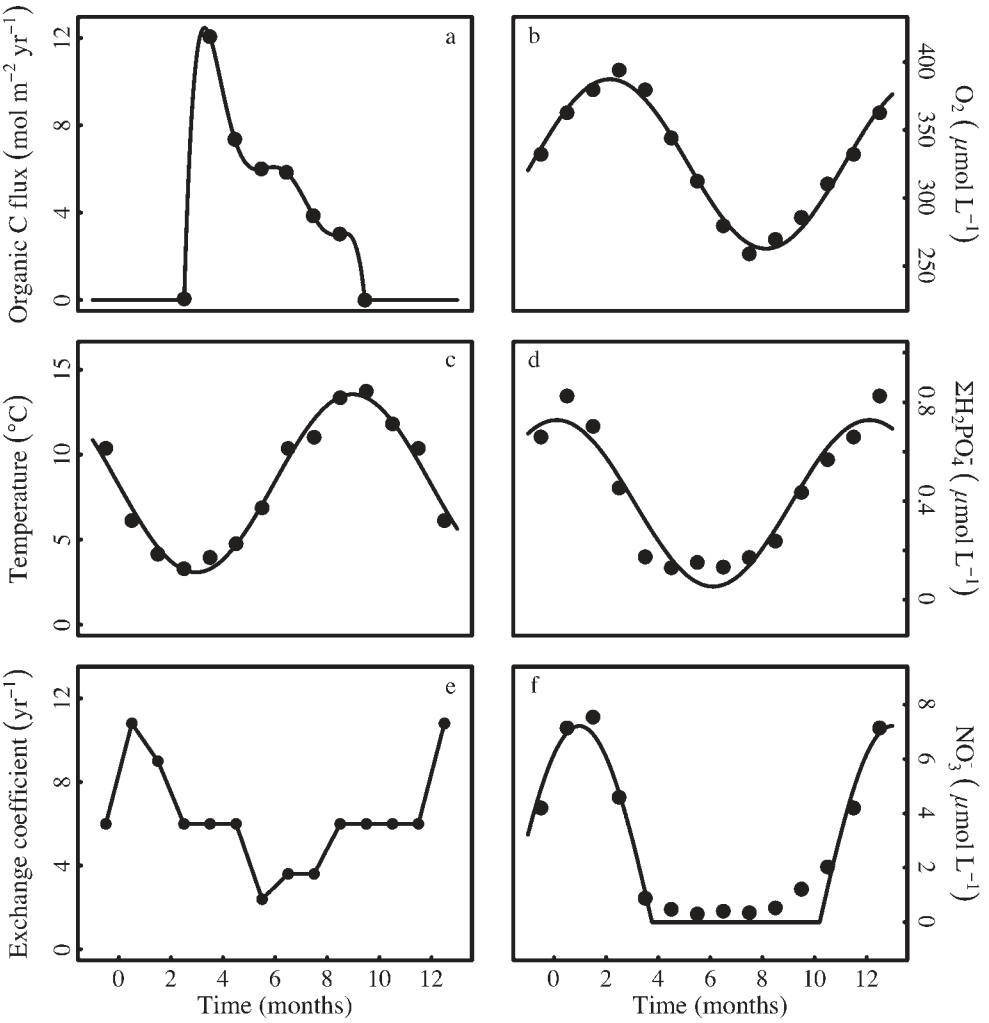

Fig. 1. Temporally variable model forcing functions: (a) depositional flux of organic carbon; (b) source water oxygen concentration; (c) bottom-water temperature; (d) source water phosphate concentration; (e) exchange coefficient that defines transport between source and deep water; and (f) source water nitrate concentration. Circles represent field data (*see* text for the sources of these data) and the solid line shows functions fit to the data that are supplied to the model.

regarding the sediment and pore-water data are described in full by Mort et al. (2010).

Parameter selection and boundary conditions—A number of parameters are required by the model. Bottom-water temperature, deposition of organic matter, and water-column mixing, as well as source concentrations of oxygen, nitrate, and phosphate, are all described in the model by prescribed functions (Fig. 1). In the case of temperature and source concentrations, these functions are defined by fitting a simple sinusoid function to data for site BY2 from the Baltic Environmental Database at Stockholm University (Fig. 1b–d, f). Temperature affects molecular diffusion coefficients according to relationships published by Van Cappellen and Wang (1995), as well as biodiffusive mixing (*see* below). The temperature dependencies of all reactions considered by the model are not well-constrained and are, therefore, omitted. Nevertheless, simulations were undertaken to explore the consequences of neglecting temperature effects—modeled using Q_{10} values of 1–3—and demonstrated that such dependencies have little bearing on the dynamics of the system.

To resolve constants of integration, boundary conditions must be supplied to the diagenetic module that specify how sediments interact with the overlying water column and sediment beneath the model domain. For all particulate species, a depositional flux is prescribed at the sediment–water interface and material is lost by burial alone at the base of the considered sediment column. Depositional fluxes are comprised of two components: a prescribed flux from surface waters and a flux due to the precipitation of solids in the deep-water layer. The deposition of organic material, and iron and manganese oxyhydroxides is discussed below. A depositional flux is assumed to account for the abundance of authigenic phosphorus at the sediment–water interface (Slomp et al. 1996). All other

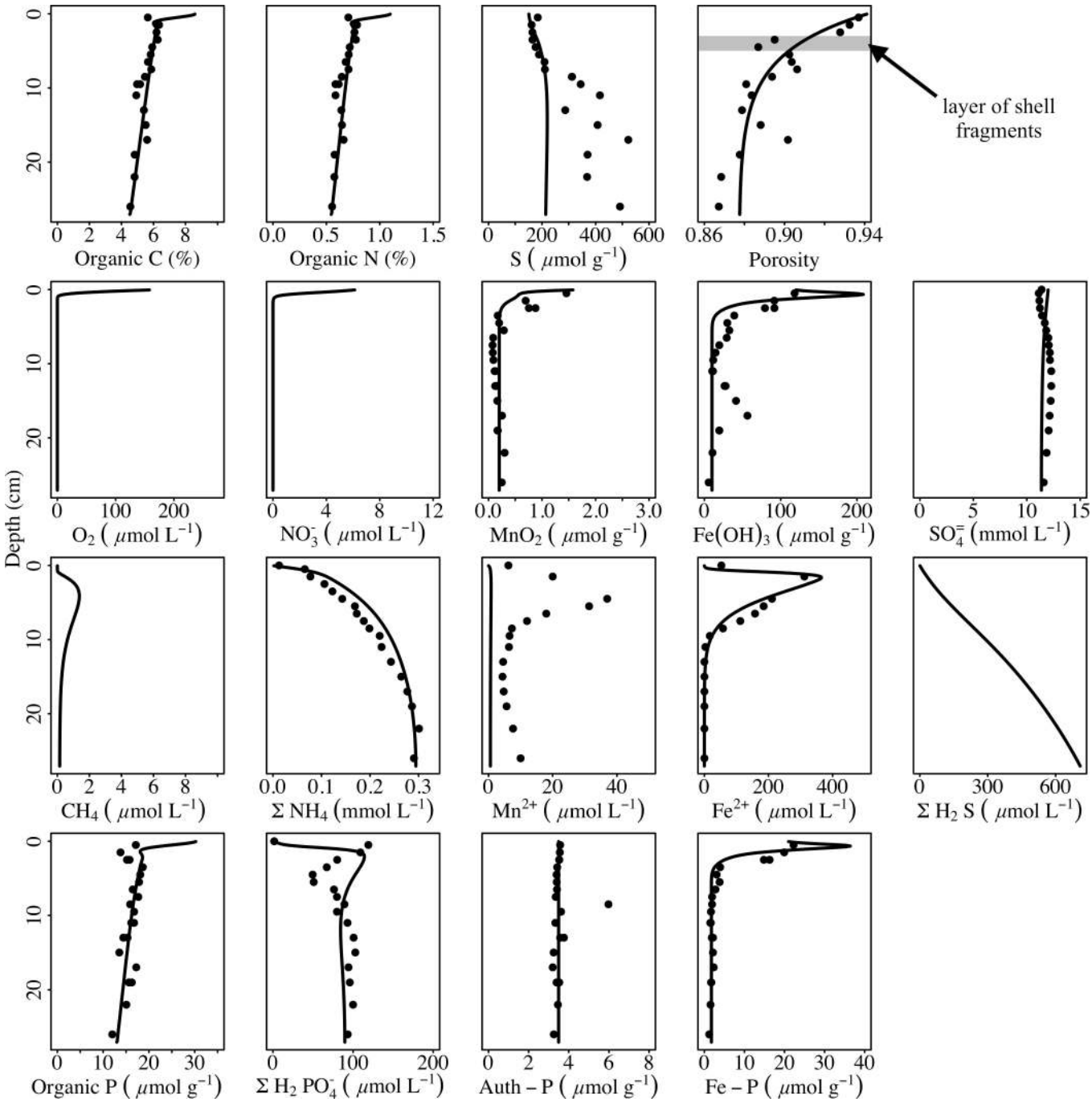

Fig. 2. Sediment and pore-water profiles. Circles are measurements made in the Arkona Basin (Sta. BY2 at 47-m depth in September 2007) taken from Mort et al. (2010); solid lines represent model output.

particulate species have a depositional flux of zero. Solutes—with the exception of H_2S—are assumed to have a gradient of zero at depth. Hydrogen sulphide, however, has a prescribed flux at the lower boundary to represent the upward diffusion due to production below the model domain. At the sediment–water interface, all solute concentrations are set to bottom-water concentrations. All boundary conditions are given in Table 7.

The deep waters of the Arkona basin are comprised mostly of saline water from the Danish Straits that intrudes as dense gravity currents. To estimate nutrient and oxygen concentrations of these intruding waters we employ a channel model (Gustafsson 2004) to compute daily flows through the Straits. Flow-weighted monthly mean concentrations in the surface waters of the Sound and Fehmarn Belt are computed from field data. Observations are only included in this calculation when the direction of flow is toward the Arkona basin; consequently, we neglect turbulent vertical mixing of Arkona surface waters into the intruding waters in this relatively simplistic description

Table 7. Boundary conditions for the diagenetic component of the model. Fluxes are in mmol m^{-2} yr^{-1} and concentration gradients are in mmol L^{-1} cm^{-1}. Organic fluxes (OF) are determined from a sixth-order polynomial fit to data from Stigebrandt (1991). *See* Parameter selection and boundary conditions section and Fig. 1a for details. For coupled concentration (CC) boundary conditions, concentrations at the boundary are set at the calculated bottom-water concentration. Coupled flux (CF) boundary conditions comprise of a flux due to precipitation of material in the deep-water layer in addition to a constant flux from surface waters. Prescribed flux (PF) boundary conditions only comprise of a constant flux. L denotes the extent of the sediment domain in the model (cm).

	Boundary conditions	
Component	$x=0$	$x=L$
C^{α}_{org}	OF (*see* text and Fig. 1a)	$\frac{\partial[C^{\alpha}_{org}]}{\partial x}=0$
C^{β}_{org}	OF (*see* text and Fig. 1a)	$\frac{\partial[C^{\beta}_{org}]}{\partial x}=0$
C^{γ}_{org}	OF (*see* text and Fig. 1a)	$\frac{\partial[C^{\gamma}_{org}]}{\partial x}=0$
P^{α}_{org}	OF (*see* text and Fig. 1a)	$\frac{\partial[P^{\alpha}_{org}]}{\partial x}=0$
P^{β}_{org}	OF (*see* text and Fig. 1a)	$\frac{\partial[P^{\beta}_{org}]}{\partial x}=0$
P^{γ}_{org}	OF (*see* text and Fig. 1a)	$\frac{\partial[P^{\gamma}_{org}]}{\partial x}=0$
O_2	CC	$\frac{\partial[O_2]}{\partial x}=0$
NO^{-}_{3}	CC	$\frac{\partial[NO^{-}_{3}]}{\partial x}=0$
MnO^{α}_{2}	CF; $J_{MnO^{\alpha}_{2}}=0.03$	$\frac{\partial[MnO^{\alpha}_{2}]}{\partial x}=0$
MNO^{β}_{2}	PF; $J_{MnO^{\beta}_{2}}=0$	$\frac{\partial[MnO^{\beta}_{2}]}{\partial x}=0$
$Fe(OH)^{\alpha}_{3}$	CF; $J_{Fe(OH)^{\alpha}_{3}}=57.5$	$\frac{\partial[Fe(OH)^{\alpha}_{3}]}{\partial x}=0$
$Fe(OH)^{\beta}_{3}$	PF; $J_{Fe(OH)^{\beta}_{3}}=0$	$\frac{\partial[Fe(OH)^{\beta}_{3}]}{\partial x}=0$
$SO^{=}_{4}$	CC	$\frac{\partial[SO^{=}_{4}]}{\partial x}=0$
Mn^{2+}	CC	$\frac{\partial[Mn^{2+}]}{\partial x}=0$
Fe^{2+}	CC	$\frac{\partial[Fe^{2+}]}{\partial x}=0$
ΣNH^{+}_{4}	CC	$\frac{\partial[\Sigma NH^{+}_{4}]}{\partial x}=0$
ΣH_2S	CC	$J_{H_2S}=-50$
CH_4	CC	$\frac{\partial[CH_4]}{\partial x}=0$
$\Sigma H_2PO^{-}_{4}$	CC	$\frac{\partial[\Sigma H_2PO^{-}_{4}]}{\partial x}=0$
S_0	PF; $J_{S_0}=0$	$\frac{\partial[S_0]}{\partial x}=0$
FeS	CF; $J_{FeS}=0$	$\frac{\partial[FeS]}{\partial x}=0$
FeS_2	PF; $J_{FeS_2}=0$	$\frac{\partial[FeS_2]}{\partial x}=0$
Fe–P^{α}	CF; $J_{Fe-P^{\alpha}}=\chi J_{Fe(OH)^{\alpha}_{3}}$	$\frac{\partial[Fe-P^{\alpha}]}{\partial x}=0$
Fe–P^{β}	PF; $J_{Fe-P^{\beta}}=0$	$\frac{\partial[Fe-P^{\beta}]}{\partial x}=0$
Auth–P	PF; $J_{Auth-P}=4.27$	$\frac{\partial[Auth-P]}{\partial x}=0$

of a markedly dynamic sea. Source concentrations of all other solutes are assumed to be constant; most are zero with the exception of sulphate (12 mmol L^{-1}) and ammonium (0.18 μmol L^{-1}). The renewal of Arkona deep water is episodic and, thus, exchange with the deep-water layer is seen from the perspective of an average annual cycle in the model. Salinity does not exhibit a clear seasonal cycle and, consequently, does not serve as a good proxy for the time scale of deep water. Nevertheless, because the water column is strongly stratified throughout the year, temperature fluctuations are chiefly due to lateral exchange and thereby provide a good indication of the through-flow. Also, short-term variability in temperature in the source waters is comparatively small compared to the amplitude of the annual cycle, which is certainly not the case for salinity. Thus, the exchange coefficient for Arkona deep water (i.e., Fig. 1e) is estimated by tuning to reproduce observed bottom-water temperatures at BY2. This estimation is independent of the depth of the deep-water layer used by the model, which in turn cannot be derived from sparsely spaced observations. Therefore, the depth of the deep-water layer is used as a tuning parameter of the model.

Deposition of organic matter is described using a sixth-order polynomial fit to estimates of primary production in the Arkona basin (Fig. 1a; Stigebrandt 1991). Productivity peaks at the end of March due to the spring bloom, then declines throughout the year and is zero throughout the winter months. Stigebrandt (1991) derived these estimates from data taken from the International Council for the Exploration of the Sea database for the interval 1957 to 1982. These figures are low relative to other estimates (Wasmund et al. 2001) and the organic-matter deposition function must, therefore, be scaled up in order to reproduce sedimentary organic-matter profiles. The model was spun-up for 800 yr before all model runs to ensure a quasi–steady-state at the outset. Simulations ran from 80 yr ago until present day. Over this period organic loading is assumed to increase linearly, having a scaling factor of 1.5 at the outset and 2.3 at the end of the simulation, to reflect an increase in nutrient availability. For example, Savchuk

et al. (2008) estimate basin-wide annual averages of dissolved inorganic phosphorus concentrations have increased by a factor of 1.25–2.5 over the past century. Sediment profiles show C : N and C : P ratios that are fairly constant with depth, around 10 : 1 and 290 : 1, respectively. Assuming that the highly reactive pool of organic matter is remineralized entirely close to the sediment–water interface, these ratios reflect the composition of the less reactive and inert organic pools and are used accordingly in the model. The C : N : P ratio of the highly reactive pool has a prescribed value of 106 : 16 : 1, that is, the Redfield ratio. The depositional fluxes of organic nitrogen and phosphorus are determined by combining the C : N and C : P ratios with the organic flux function after it has been divided into its constituent pools.

The vast majority of sedimentary parameters used by the model are known a priori from the data set, literature, or empirical relationships (Tables 3 and 4). Nonetheless, there remain a small number of parameters that need to be constrained by fitting model output to observations, that is, sediment and pore-water profiles from Mort et al. (2010). The value of Ψ was estimated for BY2 by fitting the model-generated ammonium profile to field measurements, because ammonium is produced by sulphate reduction at depth. Sulphate is also consumed during this reaction and, therefore, the sulphate profile provides an additional check that sulphate reduction is not overestimated. Methanogenesis plays but a minor role in ammonium production at the considered site and depth in the sediment, because sulphate is not exhausted over the modeled domain.

There are no existing estimates of biodiffusive mixing rates at the Arkona site and, therefore, a value is estimated by fitting the model output to measured sediment profiles (detailed below). Because faunal metabolism is a function of bottom-water temperature (Ouellette et al. 2004), bioturbation is assumed to be a linear function of temperature. Lowest temperatures occur at BY2 in March immediately prior to the spring bloom. At this time of year, the activities of the benthic community have not only declined due to the low temperatures, but also because the flux of fresh organic matter to the sediments ceased $\sim$ 6 months earlier. This provides further justification for assuming bioturbation is negligible in March. In contrast, August is the warmest time of year and is preceded by 6 months of sustained deposition of labile organic matter. The maximal rate of bioturbation is accordingly assumed to occur at this time of year.

The magnitude of the maximum biodiffusion coefficient is determined by considering the dissolved iron and iron oxyhydroxide profiles. Biogenic mixing transports iron and manganese oxyhydroxides and organic matter downward into the sediment. Beyond the penetration depths of oxygen and nitrate, organic matter is decomposed by means of iron and manganese reduction. The depositional flux of iron oxyhydroxides and rate of bioturbation can, thus, be estimated by adjusting these parameters so that the model replicates Fe^{2+} and $Fe(OH)_3$ profiles. After determining the biodiffusion coefficient, the depositional flux of manganese oxyhydroxides in the model is then chosen to reproduce the measured profile.

In addition to food availability and temperature, benthic macrofauna are also affected by the redox conditions of the overlying waters. Bottom-water oxygen concentrations have been shown to have a significant influence on the depth of bioturbation (Smith et al. 2000). To simulate such behavior, the mixing depth in the model is defined as a linear function of bottom-water oxygen, reaching a maximum when the deep-water concentration is the same as the source concentration and a minimum when the deep layer becomes anoxic.

Finally, the depth of the deep-water layer was chosen so as to reproduce the time series for bottom-water solutes and the rate of nitrification in the water column was reduced by 10^{-2} relative to sedimentary nitrification to achieve a good fit. This reflects a lower bacterial density in the overlying water (i.e., 10^9–10^{10} cells mL^{-1} bulk sediment [Burdige 2006] and 10^6 cells mL^{-1} water in Arkona bottom waters [Heinänen 1991]). An additional oxygen sink of 0.3 mmol L^{-1} yr^{-1} was included in the deep-water layer in order to replicate the bottom-water oxygen time series. This sink accounts for factors that are not explicitly described by the model, such as respiration in the water column and spatial variability in benthic oxygen demand within the basin (i.e., higher O_2 consumption at other sites). The grid size of the sediment is set at 1 mm.

Results

Results of the simulation described above are presented in Figs. 2–7. Figure 2 plots observed sediment and pore-water profiles sampled at BY2 in September 2007 by Mort et al. (2010) with profiles generated by the model for that the sampling date. Bottom-water time series for oxygen, phosphate, nitrate, and ammonium concentrations generated by the model over the final year of the simulation are plotted in Fig. 3 with field data from the Baltic Environmental Database at Stockholm University for comparison. Because organic-matter degradation drives the geochemistry of marine sediments, Fig. 4 shows how the remineralization rate fluctuates over the final year of the simulation and the contribution of different oxidants to the decomposition of organics. The oxygen budgets for both bottom waters and underlying sediments are given in Fig. 5. Figure 6 plots the phosphorus fluxes between the sediment and water column over a period of a year, while Fig. 7 details sedimentary phosphorus cycling during this interval.

Discussion

Bottom-water and sediment chemistry—Figure 2 shows observed sediment and pore-water profiles at BY2 from September 2007 (Mort et al. 2010), and model-generated profiles at the same time of year. Comparing the model output to field data suggests that, for the most part, the model is able to describe the sedimentary biogeochemical dynamics at BY2 very well. There are, however, some discrepancies that require comment. First, the model is unable to reproduce the peak in dissolved manganese present near the sediment–water interface, unless the surface concentration of MnO_2 is unreasonably high.

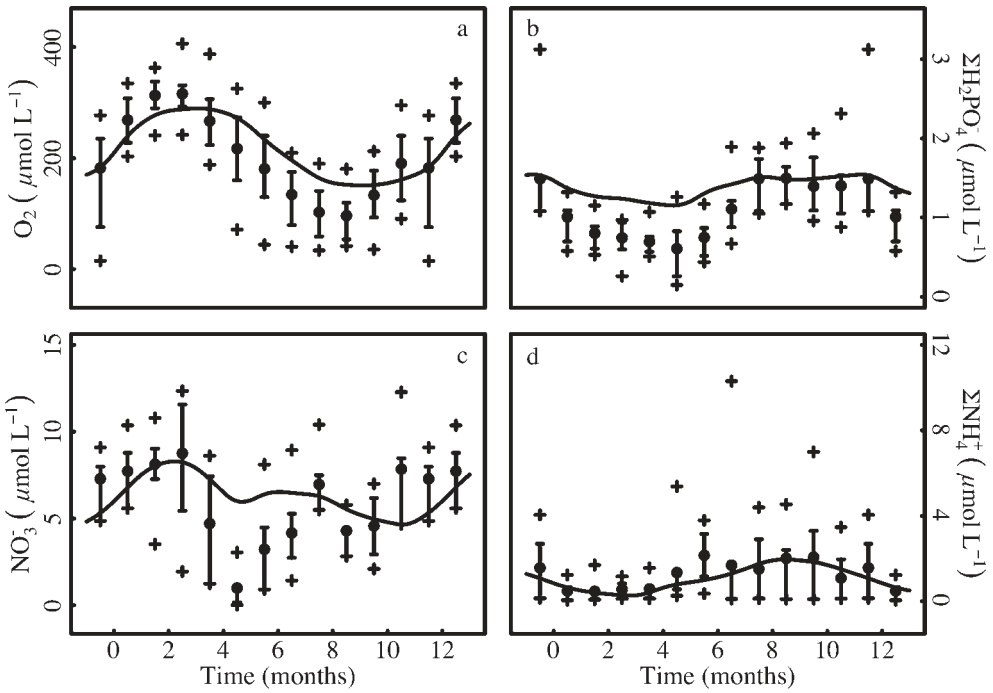

Fig. 3. Time series of bottom-water solutes: (a) oxygen, (b) phosphate, (c) nitrate, and (d) ammonium. Circles represent averaged monthly concentrations observed at BY2, 45-m depth, with bars denoting the 20% and 80% quantiles, and crosses marking maximum and minimum values. All data were obtained from the Baltic Environmental Database at Stockholm University. Solid lines represent model output.

Previous diagenetic studies of seasonally variable environments have experienced the same issue (Canavan et al. 2006), suggesting an incomplete understanding of manganese cycling under transient conditions. Nevertheless, because manganese oxide does not exert a significant influence on organic-matter remineralization when compared to other oxidants, such as oxygen and iron oxyhydroxides (*see* Organic-matter remineralization section), it does not significantly affect model results. Also, at depth the simulated profile of solid phase sulphur (S_0 + FeS + FeS_2) differs somewhat from observations: the measured profile shows a great deal of variability below 10 cm and the amount of particulate sulphur present—most likely as pyrite—is underestimated by the model. A possible explanation is that the depositional flux of iron oxyhydroxides was higher in the past, supplying more iron for pyrite formation and that this flux was also highly variable. Time series and profiles of phosphorus species are reproduced in the absence of the precipitation of a mineral phase (e.g., apatite). This together with a vertical 'authigenic' phosphorus profile suggests that all authigenic phosphorus is actually deposited at BY2 at a constant rate, as opposed to being formed in situ.

The porosity profile at station BY2 is typical of a muddy sediment, decreasing exponentially with increasing sediment depth toward an asymptote (Fig. 2). Within the model, porosity is represented by a standard function that is fit to field data and, in general, provides a good description of observations. Nevertheless, the function overestimates porosity between 3 cm and 5 cm, a somewhat compacted region that is littered with shell fragments. The downward diffusion of phosphate from the peak near the sediment–water interface is impeded by the presence of shell fragments and a lower than estimated porosity. As a result, the phosphate peak disperses downward slower in the field than is predicted by the model. The heterogeneous nature of sediments imply, however, that this is a core-specific effect and is not representative of the entire deep

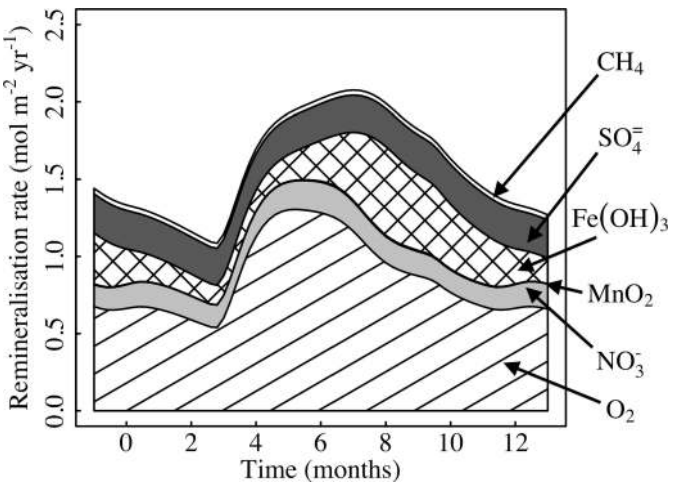

Fig. 4. Seasonal variation in organic-matter remineralization pathways: aerobic respiration (O_2); denitrification (NO_3^-); manganese reduction (MnO_2); iron reduction ($Fe(OH)_3$); sulphate reduction ($SO_4^=$); and methanogenesis (CH_4).

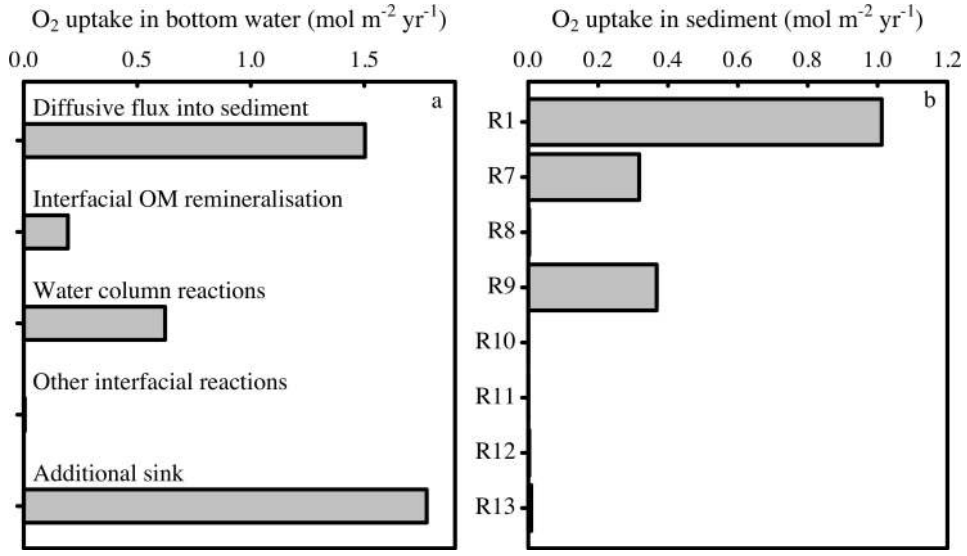

Fig. 5. Annual oxygen uptake in (a) bottom waters and (b) the sediment column of the model. Oxygen sinks in the deep layer of the water column are ([a], top to bottom) diffusive flux into sediment, organic-matter (OM) remineralization at the sediment–water interface, reactions in the water column (i.e., the deep-water layer), other reactions at the sediment–water interface besides aerobic respiration, and an additional sink representing processes not explicitly described by the model. In the sediment column, oxygen is consumed by reactions. Table 2 states the reactions referred to by (b).

basin. Indeed, no other phosphate profiles observed to date in the Baltic Sea exhibit a marked minimum at intermediate depths (Carman and Rahm 1997; Mort et al. 2010). Bioirrigation cannot account for this observation at BY2 because an exchange of pore water with overlying waters not only expels phosphate, but also introduces oxygenated water to the uppermost sediment attenuating dissimilatory iron reduction and, therefore, the dissolved iron and phosphate peaks. Despite the differences between the modeled and measured phosphate profile at intermediate depths in the sediment discussed above, the model still provides a reasonable description of the phosphate gradient at the sediment–water interface—and, therefore, a reasonable estimate of the benthic efflux. Note that the site considered is located in a highly dynamic region of the Baltic Sea, as is evident from the seasonal and inter-annual variability observed in deep-water solute concentrations (Fig. 3) and the marked variability in pore-water phosphate in response to bottom-water conditions. The measured peak in pore-water phosphate near the surface is, thus, a highly transient feature (inset profiles of Fig. 6a).

Figure 3 shows that despite a simple parameterization of deep-water exchange, the model provides a good description of the seasonal variability in bottom-water oxygen and phosphate concentrations. In addition, the model reproduces the observed trends in bottom-water ammonium and nitrate concentrations well.

Organic-matter remineralization—The pathways through which organic matter is decomposed vary seasonally depending on the availability and distribution of oxidants and reactive organic material. The majority of remineralization occurs by means of aerobic respiration with a maximum occurring shortly after the deposition of the spring bloom when both labile organic matter and oxygen are readily available (Fig. 4). Bottom-water oxygen declines as a result of benthic consumption and a decrease in bottom-water exchange in the summer months due to calmer conditions and enhanced stratification (Fig. 1e). Furthermore, bioturbation gradually mixes labile organic matter deeper into the sediment beyond the penetration depth of oxygen, allowing organic-matter remineralization to progress by other pathways. Biogenic mixing also transports manganese and iron oxyhydroxides downward where—upon nitrate depletion—they are employed in organic-matter oxidation. In contrast to iron oxyhydroxides, manganese oxyhydroxides are found at relatively low concentrations and, therefore, play only a minor role in the degradation of organic matter. Consequently, after the decline in aerobic respiration iron reduction is seen to increase as both labile organic material and amorphous iron oxyhydroxides are mixed downward by benthic fauna (Fig. 4). Any organics escaping oxidation by these pathways are subject to sulphate reduction as they are buried, which occurs at a steady rate throughout the year. Because sulphate is abundant over the considered depth, methanogenesis contributes only a very small amount to the decomposition of organic matter. In summary, Fig. 4 shows that aerobic respiration is the dominant remineralization pathway at BY2 with sulphate reduction, iron reduction, and denitrification playing secondary roles, while other pathways are of negligible importance, as has been observed in diagenetic studies at other sites (Berg et al. 2003).

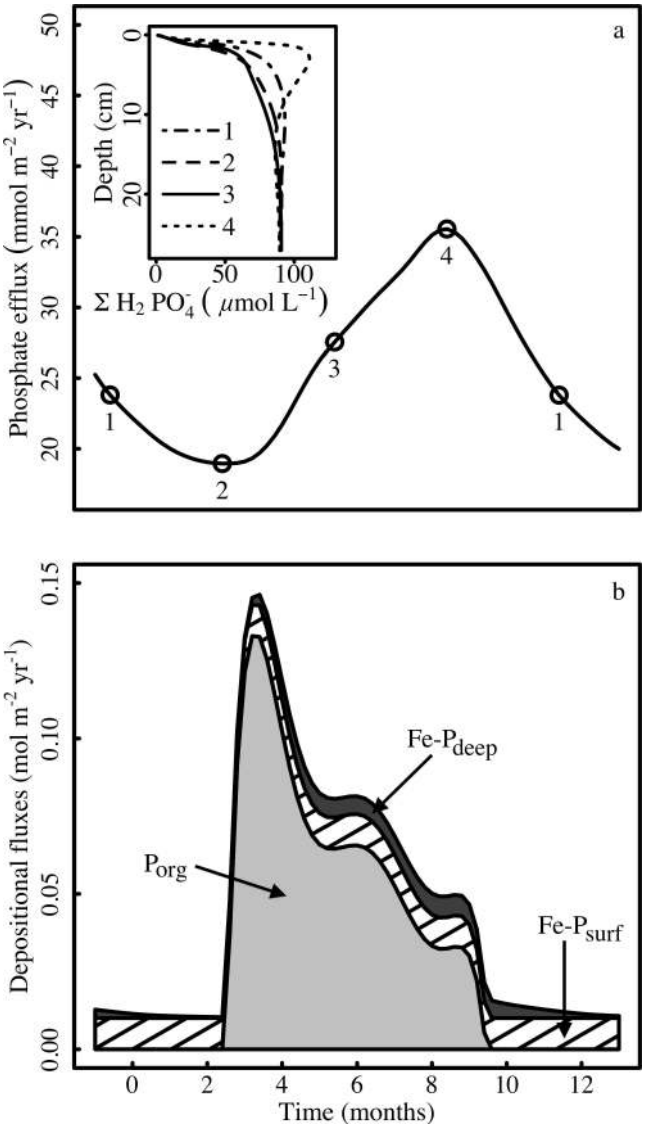

Fig. 6. The annual variation in phosphorus fluxes in the model. (a) shows the efflux of phosphate from the sediment into bottom waters. Inset are pore-water phosphate profiles throughout the year. These profiles are numbered and correspond to the numbered points on efflux plot. (b) plot shows the depositional flux of phosphorus at the sediment–water interface broken down into its constituent parts: organic phosphorus (P_{org}); iron-bound phosphorus from surface waters (Fe–P_{surf}); and iron-bound phosphorus precipitated in bottom waters (Fe–P_{deep}).

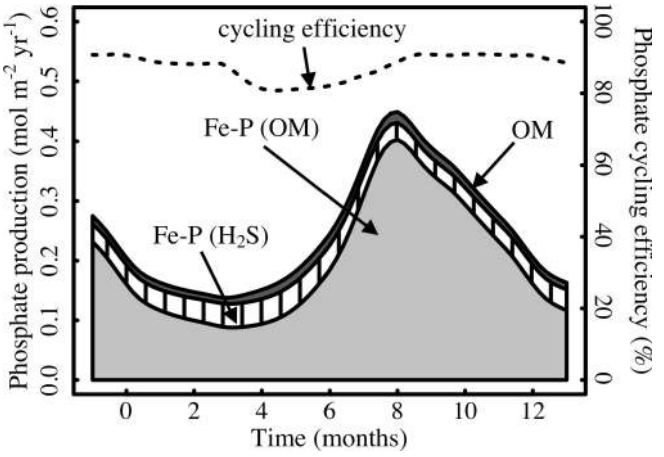

Fig. 7. Seasonal variation in phosphate production by diagenetic reactions: remineralization of organic matter (OM); dissolution of iron oxyhydroxides during dissimilatory iron reduction (Fe–P (OM)); and dissolution of iron oxyhydroxides during iron reduction by hydrogen sulphide (Fe–P (H_2S)). The dotted line represents cycling efficiency, which is defined as the percentage of phosphate produced at a time that is taken up by iron oxyhydroxide formation.

Oxygen consumption pathways—To explore the role sediments play in the evolution of bottom-water redox conditions, annual oxygen budgets were constructed using the model. Two such budgets are considered pertaining to oxygen utilization within the deep-water layer and the sediment column. Oxygen is removed from the deep-water layer by four mechanisms: reactions in the water (e.g., nitrification, iron oxyhydroxide precipitation), diffusive flux into the sediment, oxidation of organic material at the sediment–water interface, and nonorganic reactions at the sediment–water interface. An additional oxygen sink is included to account for higher benthic oxygen uptake elsewhere in the basin, aerobic respiration within the water column, and other processes that consume oxygen but are not accounted for explicitly in the model. Oxygen uptake in the sediment column, however, is due solely to reactions.

Oxygen removal from the deep-water layer—Figure 5a shows that sedimentary pathways account for a significant proportion of oxygen uptake in the bottom-water layer, illustrating the important role sediments play in oxygen dynamics at the site. Of the oxygen consumed by sediments, most diffuses into the sediment to react below the sediment–water interface. Remineralization of organic matter at the sediment–water interface accounts for around 5% of the annual uptake of oxygen from the deep-water layer and releases ammonium directly into the water column. In addition, periods of low oxygen lead to a shoaling in the oxygen penetration depth allowing other reduced species to diffuse out of the sediment into the water column. Because such periods coincide with a decline in exchange in the water column, these species are not exported effectively and are able to build in bottom waters consuming any oxygen that is present. When mixing increases once again in winter months, these species are either exported from deep waters or oxidized by the renewed input of oxygen. Oxidation of reduced species entering the water column by either molecular diffusion or interfacial reactions, therefore, represents a notable sink for oxygen in bottom waters (Fig. 5a). The additional bottom-water oxygen sink likely reflects higher benthic oxygen demand elsewhere in the Arkona basin, due to the heterogeneous nature of sediments, and degradation of organic matter in the water column, which is not modeled explicitly within the deep waters. Gustafsson and Omstedt (2009) estimated oxygen uptake due to respiration in waters below the thermocline in the Arkona basin at 10 mL L^{-1} yr^{-1}, which is comparable to our estimate of 7 mL L^{-1} yr^{-1}.

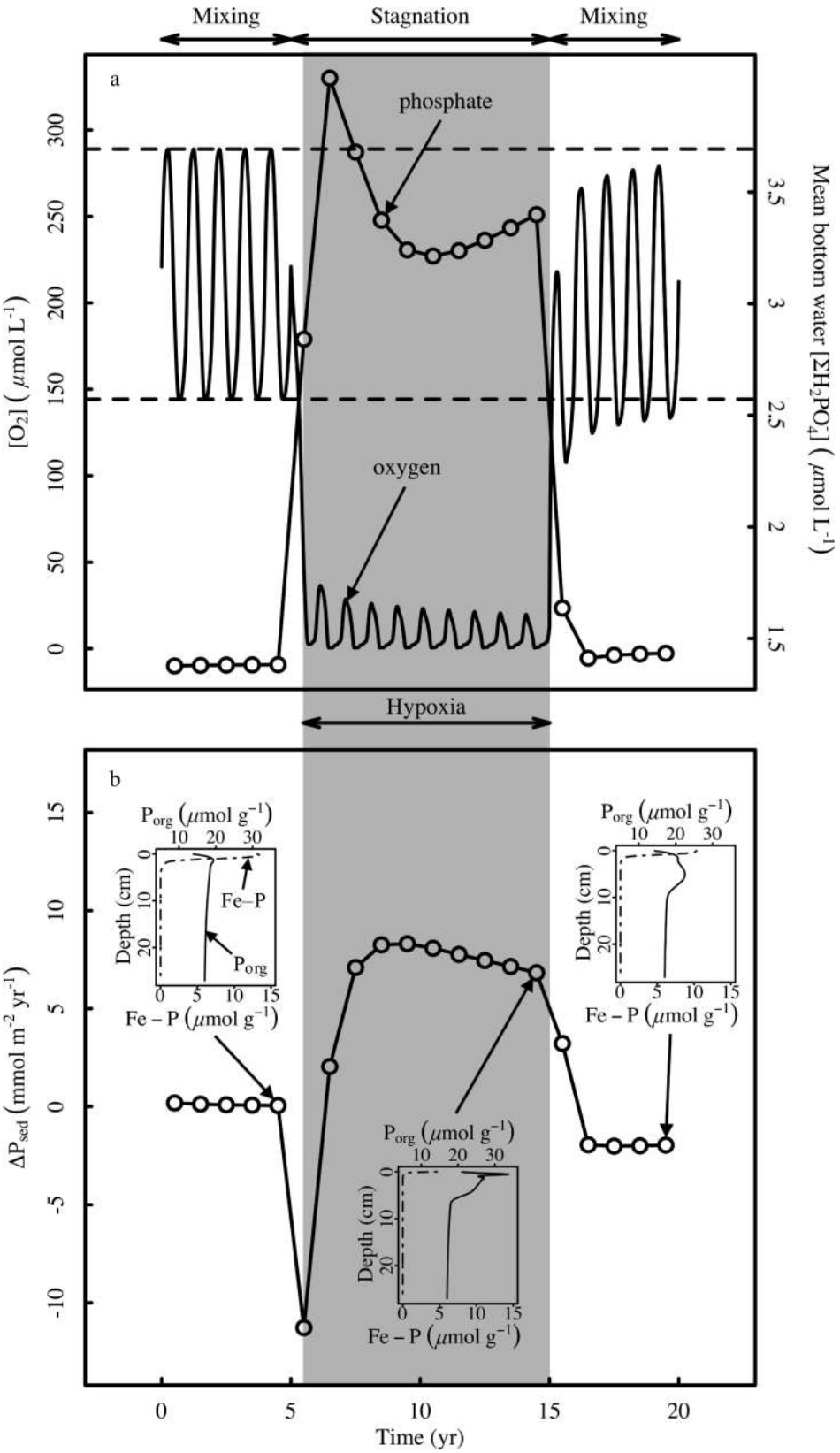

Fig. 8. A simulation of a 10-yr water-column stagnation period between two 5-yr periods of present-day mixing conditions. (a) shows the bottom-water oxygen concentration and mean annual bottom-water phosphate concentration. The shaded region denotes hypoxia. (b) shows the annual change in depth-integrated phosphorus content of the sediment as defined by Eq. 5. Inset profiles show organic phosphorus (P_{org}; solid line) and iron-bound phosphorus (Fe–P; dot-dash line) at selected times.

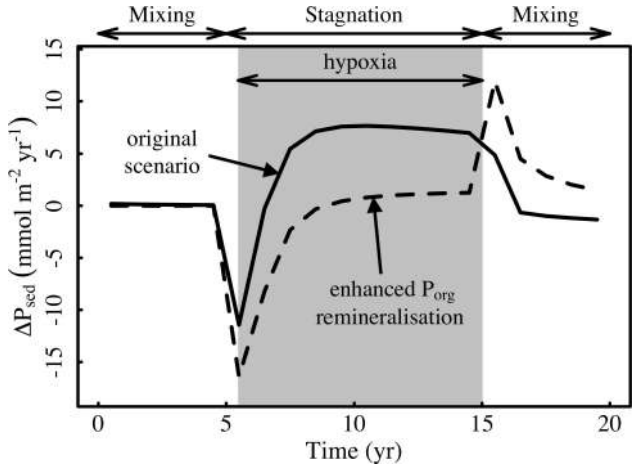

Fig. 9. The annual change in depth-integrated phosphorus content of the sediment (as defined by Eq. 5) for simulations with a 10-yr water-column stagnation period preceded and followed by a 5-yr period of present-day mixing conditions. The solid black line shows the original scenario, while the dashed line denotes a simulation with accelerated organic phosphorus remineralization under hypoxic conditions ($\varepsilon = 100$).

Oxygen uptake in the sediment column—Oxygen is used in numerous reactions in sediments, such as the oxidation of organic matter (R1), nitrification (R7), precipitation of metal oxides (R8, R9), as well as the oxidation of iron sulphide minerals (R10, R11), and other reduced species (R12, R13). Figure 5b shows the annual uptake of oxygen in the sediment region divided between these reaction pathways. The vast majority of oxygen is used in the remineralization of organic matter with the rest consumed by nitrification and iron oxyhydroxide precipitation. All other reactions are negligible in their contributions to oxygen uptake. Together with the oxygen budget for the deep-water layer described above, these results demonstrate that one of the most prominent oxygen sinks in the system is the oxidation of organic matter beneath the sediment–water interface, which accounts for 60% of oxygen uptake within the sediment. Ammonium produced by organic-matter degradation below the sediment–water interface diffuses upward toward the water column either undergoing nitrification in the oxic region of the sediment column or escaping into the overlying water. Due to the magnitude of ammonium produced nitrification is an important process when considering oxygen uptake, representing almost 20% of the sedimentary oxygen budget (Fig. 5b).

In the considered setting, iron oxyhydroxides play an important role in the oxidation of organic matter (Fig. 4) and phosphorus dynamics. As a result of rapid iron cycling, oxidation of dissolved iron is the second largest sink for oxygen within the sediment (Fig. 5b). Iron oxyhydroxide formation is coupled to dissimilatory iron reduction: biogenic mixing transports iron oxyhydroxides beyond the oxic zone where they are reduced producing dissolved iron, which either diffuses downward to form iron sulphides or upward to form $Fe(OH)_3$, thus perpetuating the cycle. In addition to bioturbation, the depth of the redox boundary varies by $\sim$ 1 cm throughout the year, which enhances the importance of iron reduction.

Phosphorus cycling—Sedimentary phosphorus dynamics are highly dependent on depositional fluxes of organic matter and iron-bound phosphorus, as well as bottom-water redox conditions. To gain insight into the interplay between sediments and overlying waters with regard to phosphorus cycling, transport of phosphorus across the sediment–water interface—such as deposition of organics and phosphate efflux—is examined during the annual cycle, as well as the transformation of phosphorus species due to chemical reactions (Figs. 6 and 7). Figure 6b shows that the deposition of organic matter is the chief input of phosphorus to sediments, with a peak following the spring bloom declining to zero in the autumn. Also shown in Fig. 6b is a prescribed constant rain of iron-bound phosphorus from surface waters in addition to a flux of phosphate scavenged from bottom water by the precipitation of iron oxides. There is an increase in the latter during late summer when dissimilatory iron reduction is at its greatest (Fig. 4) and oxygen penetration into the sediment has declined, allowing iron and phosphate to diffuse out of the sediments and subsequently precipitate in the water column. Phosphate efflux increases markedly at this time (Fig. 6a). The disequilibrium between the efflux of phosphate from the sediment and the scavenged depositional flux of iron-bound phosphorus results in a build-up of phosphate in bottom waters (Fig. 3b), as well as an export of phosphate to surface waters through vertical mixing. Such an export provides a source of phosphorus for primary producers.

Figure 7 shows that hydrogen sulphide diffuses upward and reduces iron oxyhydroxides, thus liberating associated phosphorus. In addition, dissimilatory iron reduction increases after the spring bloom and phosphate is released from both organic matter and iron oxyhydroxides. Phosphorus cycling efficiency, that is, the percentage of phosphate produced in sediments that is bound by the diagenetic formation of iron oxyhydroxides, is high all year round, with an average of 87.5% (Fig. 7). Consequently, phosphate release from iron oxyhydroxides during dissimilatory iron reduction dominates phosphate production in sediments due to efficient cycling (Fig. 7).

Transition into sustained hypoxia, recovery, and legacy—As hypoxic regions in the Baltic Sea expand, sediments that previously were overlain by oxic (or seasonally oxic) bottom waters are subject to prolonged periods of oxygen deprivation, altering phosphorus cycling (Conley et al. 2002; Mort et al. 2010). In addition to illuminating the dynamics of sediment geochemistry under present-day conditions, the coupled benthic–pelagic model is able to provide insight into the response of sediments to the onset of long-term hypoxia and subsequent recovery. The scenario considered here assumes the water column stagnates for a period of 10 yr, simulated in the model by reducing η, the deep-water exchange coefficient, to 20% of its previous values. Prior to stagnation the model is run to steady-state using parameters relating to present-day conditions. The model is then run for 5 yr before stagnation occurs and for an additional 5 yr after this period with present-day mixing conditions. By doing so, the model is

driven into year-round hypoxia—by retarding the ventilation of bottom waters—and is then allowed to recover when exchange resumes at present-day levels.

Figure 8a shows the bottom-water oxygen and phosphate concentrations during the scenario. The shaded region represents the period when bottom waters are hypoxic. Plotted beneath in Fig. 8b is the annual change in depth-integrated phosphorus content of the sediment (ΔP_{sed}), where

$$P_{sed} = \int_0^L \left(P_{org} + Fe - P + Auth - P + \sum H_2PO_4^- \right) dx \quad (5)$$

and L is the extent of the sediment domain. At the onset of hypoxia, there is a large pulse of phosphate corresponding to the liberation of iron-bound phosphorus during dissimilatory iron reduction that is not subsequently retained by the formation of iron oxyhydroxides due to the absence of oxygen. The model predicts an initial diffusive efflux of ~ 3 g P m^{-2} due to hypoxia (results not shown), which is comparable to previous estimates (e.g., 3 g P m^{-2}, [Gustafsson and Stigebrandt 2007]; 2 g P m^{-2}, [Eilola et al. 2009]). These results are in agreement with observations that change in the phosphate pool in the water column correlates with the area of hypoxic bottom waters (Conley et al. 2002). The loss of Fe–P from the sediment is evident in Fig. 8b, but sedimentary phosphorus content soon increases due to the formation of an organic-rich layer as a result of enhanced organic-matter preservation under hypoxic conditions.

Following reventilation of bottom waters and a return to seasonally hypoxic conditions, benthic oxygen demand is greater than prior to the stagnation period due to the presence of an organic-rich layer at the sediment–water interface and, as a result, bottom-water oxygen does not immediately return to the concentration observed before the onset of hypoxia. Indeed, even after 5 yr the system has not returned to its previous state, illustrating the so-called 'legacy of hypoxia' (Turner et al. 2008). The organic-rich layer remains evident at the end of the simulation and the concentration of iron-bound phosphorus is yet to return to its prehypoxia value (right-hand inset profile in Fig. 8b). After reoxygenation of the overlying waters, ΔP_{sed} becomes negative, reflecting the oxidation of the organic-rich layer and associated release of phosphate. An elevated $C_{org} : P_{org}$ ratio resulting from enhanced organic phosphorus remineralization during the stagnation period, which is not accounted for in this simulation, would reduce this release of phosphate upon reoxygenation of bottom waters. Furthermore, previous studies have noted that organic phosphorus is retained during the oxic degradation of organic-rich layers deposited under anoxic conditions (Slomp et al. 2002).

Note that the large variability in the organic phosphorus profile close to the sediment–water interface during the hypoxic interval (center inset in Fig. 8b) is due to seasonal variation in the deposition of organic material (i.e., Fig. 1a) and the absence of benthic fauna to mix the sediment. In the model, numerical diffusion smooths out these signals with time, while, in nature, any physical disturbances would have the same effect because the features occur on such a small scale.

Results of the simulation agree with data from Mort et al. (2010), who observed the accumulation of an organic-rich layer and depletion of Fe–P in the sediments of site BY29 in the Northern Gotland basin of the Baltic Sea, which became hypoxic ~ 3 decades ago. Sustained oxygen depletion prolongs the time-scale of phosphorus cycling: instead of rapid cycling by iron oxyhydroxides seen earlier, phosphorus gradually accumulates in the organic-rich layer. Nevertheless, although model output shows accumulation of organic phosphorus under hypoxic conditions, enhanced remineralization of organic phosphorus relative to organic carbon (Ingall et al. 1993; Slomp et al. 2002; Mort et al. 2010) would attenuate organic phosphorus retention in the sediment during hypoxia and consequently increase the $C_{org} : P_{org}$ ratio.

A further simulation was undertaken in which ε, the acceleration factor for organic phosphorus remineralization, was set to 100 to produce elevated $C_{org} : P_{org}$ ratios of $\sim$ 300–335 in the accumulating organic-rich layer during the hypoxic period, like those reported by Mort et al. (2010). All other parameters were as in the previous scenario. Figure 9 compares ΔP_{sed} for this simulation with that of the previous simulation. Results show that under such circumstances sedimentary phosphorus is reduced throughout the stagnation period as a result of dissolution of phosphorus-bearing iron oxyhydroxides and enhanced remineralization of organic phosphorus. When exchange resumes in the water column, bottom waters are reoxygenated, precipitating iron oxyhydroxides that bind phosphate in the bottom waters and are subsequently deposited at the sediment–water interface, thus increasing the phosphorus content of the sediment.

Various engineering solutions have been proposed to mitigate hypoxia in the Baltic Sea (Conley et al. 2009*b*). These approaches often employ forced reoxygenation of bottom waters by a variety of mechanisms. To examine the consequences of such measures, the two previous scenarios (i.e., with ε equal to 1 and 100) were rerun with an alternative recovery phase. Instead of reinitiating water-column exchange during the final 5 yr of the simulation, the oxygen concentration of the deep-water layer was fixed at 289 μmol L^{-1} to represent artificial reoxygenation, which is the maximum bottom-water oxygen concentration achieved in the model with present-day conditions. At the end of the forced reoxygenation period, the depth-integrated total phosphorus content of the sediment changed by just -0.14% and 1.77% when ε was equal to 1 and 100, respectively. Nonetheless, the depth-integrated Fe–P content of the sediment had increased by 1690% in both cases. Therefore, while the total amount of phosphorus retained with the sediment remains essentially unchanged, there is a shift in how phosphorus is partitioned. Phosphorus sink-switching results from the oxidation of organic matter and pyrite releasing phosphate and dissolved iron to the pore water, respectively, which are subsequently precipitated as Fe–P. The net result is an efficient conversion of organic phosphorus to iron-bound phosphorus.

Implications—In the Baltic Sea, shrewd nutrient-management strategies are needed to address the problem of eutrophication. While reducing nutrient inputs is a clear first step, model results presented above illustrate that significant internal loading complicates the issue when considering phosphorus dynamics. Following a shift in bottom-water redox conditions phosphorus cycling enters a new mode: dissolution of phosphorus-bearing iron oxyhydroxides following the onset of hypoxia acts as a potential positive feedback by elevating primary production in overlying waters, particularly by nitrogen-fixing cyanobacteria. This rapid reduction of iron oxyhydroxides in sediments under oxygen-depleted conditions coupled with preferential organic phosphorus regeneration relative to organic carbon attenuates the sedimentary phosphorus sink, thus increasing the magnitude of the water-column phosphorous reservoir. An organic-rich layer is formed in sediments during bottom-water hypoxia, which increases the benthic oxygen demand and consequently hinders remediation. Forced reoxygenation of bottom waters reintroduces inorganic nitrogen to the water column and induces phosphorus sink-switching in the sediment, whereby organic phosphorus is converted to iron-bound phosphorus, with negligible effect on total phosphorus content. Should the system lapse into hypoxia once again, this enhanced pool of Fe–P would be quickly released to the water column as phosphate and potentially exacerbate conditions.

Acknowledgments

This work was funded by grants from the Baltic Sea 2020 Foundation, the Netherlands Organization for Scientific Research (Vidi grant to C. P. Slomp), and the EU-Bonus project HYPoxia Mitigation for Baltic Sea Ecosystem Restoration (HYPER). D. C. Reed gratefully acknowledges the hospitality of B. P. Boudreau at Dalhousie University. We thank two anonymous reviewers for their helpful comments.

References

Berg, P., S. Rysgaard, and B. Thamdrup. 2003. Dynamic modeling of early diagenesis. A case study in an Arctic marine sediment. Am. J. Sci. **303:** 905–955, doi:10.2475/ajs.303.10.905

Boudreau, B. P. 1984. On the equivalence of nonlocal and radial-diffusion models of porewater irrigation. J. Mar. Res. **42:** 731–735, doi:10.1357/002224084788505924

———. 1986. Mathematics of tracer mixing in sediments: 1. Spatially-dependent, diffusive mixing. Am. J. Sci. **286:** 161–198, doi:10.2475/ajs.286.3.161

———. 1996. A method-of-lines code for carbon and nutrient diagenesis in aquatic sediments. Comput. Geosci. **22:** 479–496, doi:10.1016/0098-3004(95)00115-8

———. 1997. Diagenetic models and their implementation: Modelling transport and reactions in aquatic sediments. Springer-Verlag.

———, and R. L. Marenelli. 1994. A modelling study of discontinuous biological irrigation. J. Mar. Res. **52:** 947–968, doi:10.1357/0022240943076902

Burdige, D. J. 2006. Geochemistry of marine sediments. Princeton Univ. Press.

Canavan, R. W., C. P. Slomp, P. Jourabchi, P. Van Cappellen, A. M. Laverman, and G. A. Van den Berg. 2006. Organic matter mineralization in sediment of a coastal freshwater lake and response to salinization. Geochim. Cosmochim. Acta **70:** 2836–2855, doi:10.1016/j.gca.2006.03.012

Carman, R., and L. Rahm. 1997. Early diagenesis and chemical characteristics of interstitial water and sediments in the deep deposition bottoms of the Baltic proper. J. Sea Res. **37:** 25–47, doi:10.1016/S1385-1101(96)00003-2

Conley, D. J., and others. 2009*a*. Hypoxia-related processes in the Baltic Sea. Environ. Sci. Technol. **43:** 3412–3420, doi:10.1021/es802762a

———, and ———. 2009*b*. Tackling hypoxia in the Baltic Sea: Is engineering a solution? Environ. Sci. Technol. **43:** 3407–3411, doi:10.1021/es8027633

———, C. Humborg, L. Rahm, O. P. Savchuk, and F. Wulff. 2002. Hypoxia in the Baltic Sea and basin-scale changes in phosphorus biogeochemistry. Environ. Sci. Technol. **36:** 5315–5320, doi:10.1021/es025763w

Diaz, R. J., and R. Rosenberg. 2008. Spreading dead zones and consequences for marine ecosystems. Science **321:** 926–929, doi:10.1126/science.1156401

Eilola, K., H. E. M. Meier, and E. Almroth. 2009. On the dynamics of oxygen, phosphorus and cyanobacteria in the Baltic Sea: A model study. J. Mar. Syst. **75:** 163–184, doi:10.1016/j.jmarsys.2008.08.009

Emerson, S., R. Jahnke, and D. Heggie. 1984. Sediment–water exchange in shallow water estuarine sediments. J. Mar. Res. **42:** 709–730, doi:10.1357/002224084788505942

Fiadeiro, M. E., and G. Veronis. 1977. On weighted-mean schemes for the finite difference approximation to the advection–diffusion equation. Tellus **29:** 512–522, doi:10.1111/j.2153-3490.1977.tb00763.x

Froelich, P. N., and others. 1979. Early oxidation of organic matter in pelagic sediments of the eastern equatorial Atlantic: Suboxic diagenesis. Geochim. Cosmochim. Acta **43:** 1075–1090, doi:10.1016/0016-7037(79)90095-4

Gilbert, M. A. 1977. The behaviour and functional morphology of deposit feeding in Macoma Balthica (Linne, 1758), in New England. J. Molluscan Stud. **43:** 18–27.

Goldberg, E. D., and M. Koide. 1962. Geochronological studies of deep sea sediments by the ionium/thorium method. Geochim. Cosmochim. Acta **26:** 417–450, doi:10.1016/0016-7037(62)90112-6

Guinasso, N. L., and D. R. Schink. 1975. Quantitative estimates of biological mixing rates in abyssal sediments. J. Geophys. Res. **80:** 3032–3043, doi:10.1029/JC080i021p03032

Gustafsson, B. G. 2001. Quantification of water, salt, oxygen and nutrient exchange of the Baltic Sea from observations in the Arkona Basin. Cont. Shelf Res. **21:** 1485–1500, doi:10.1016/S0278-4343(01)00014-0

———. 2004. Sensitivity of Baltic Sea salinity to large perturbations in climate. Clim. Res. **27:** 237–251, doi:10.3354/cr027237

———, and A. Stigebrandt. 2007. Dynamics of nutrients and oxygen/hydrogen sulfide in the Baltic Sea deep water. J. Geophys. Res. **112:** G02023, doi:10.1029/2006JG000304

Gustafsson, E. O., and A. Omstedt. 2009. Sensitivity of Baltic sea deep water salinity and oxygen concentration to variations in physical forcing. Boreal Environ. Res. **14:** 18–30.

Heinänen, A. P. 1991. Bacterial numbers, biomass and productivity in the Baltic Sea: A cruise study. Mar. Ecol. Prog. Ser. **70:** 283–290, doi:10.3354/meps070283

Ingall, E. D., R. M. Bustin, and P. Van Cappellen. 1993. Influence of water column anoxia on the burial and preservation of carbon and phosphorus in marine shales. Geochim. Cosmochim. Acta **57:** 303–316, doi:10.1016/0016-7037(93)90433-W

———, AND R. JAHNKE. 1994. Evidence for enhanced phosphorus regeneration from marine sediments overlain by oxygen depleted waters. Geochim. Cosmochim. Acta **58:** 2571–2575, doi:10.1016/0016-7037(94)90033-7

JØRGENSEN, B. B. 1978. A comparison of methods for the quantification of bacterial sulfate reduction in coastal marine sediments. 2. Calculations from mathematical models. Geomicrobiol. J. **1:** 29–51, doi:10.1080/01490457809377722

KATSEV, S., G. CHAILLOU, B. SUNDBY, AND A. MUCCI. 2007. Effects of progressive oxygen depletion on sediment diagenesis and fluxes: A model for the lower St. Lawrence River Estuary. Limnol. Oceanogr. **52:** 2555–2568, doi:10.4319/lo.2007.52.6.2555

———, B. SUNDBY, AND A. MUCCI. 2006. Modeling vertical excursions of the redox boundary in sediments: Application to deep basins of the Arctic Ocean. Limnol. Oceanogr. **51:** 1581–1593, doi:10.4319/lo.2006.51.4.1581

LEVIN, L., AND OTHERS. 2009. Effects of natural and human-induced hypoxia on coastal benthos. Biogeosciences **6:** 2063–2098, doi:10.5194/bg-6-2063-2009

LONG, W. C., B. J. BRYLAWSKI, AND R. D. SEITZ. 2008. Behavioral effects of low dissolved oxygen on the bivalve *Macoma balthica*. J. Exp. Mar. Biol. Ecol. **359:** 34–39, doi:10.1016/j.jembe.2008.02.013

MOODLEY, L., J. J. MIDDELBURG, P. M. J. HERMAN, K. SOETAERT, AND G. J. DE LANGE. 2005. Oxygenation and organic-matter preservation in marine sediments: Direct experimental evidence from ancient organic carbon-rich deposits. Geology **33:** 889–892, doi:10.1130/G21731.1

MORSE, J. W., AND P. M. ELDRIDGE. 2007. A non-steady state diagenetic model for changes in sediment biogeochemistry in response to seasonally hypoxic/anoxic conditions in the "dead zone" of the Louisiana shelf. Mar. Chem. **106:** 239–255, doi:10.1016/j.marchem.2006.02.003

MORT, H. P., C. P. SLOMP, B. G. GUSTAFSSON, AND T. J. ANDERSEN. 2010. Phosphorus recycling and burial in Baltic Sea sediments with contrasting redox conditions. Geochim. Cosmochim. Acta **74:** 1350–1362, doi:10.1016/j.gca.2009.11.016

MORTIMER, C. H. 1941. The exchange of dissolved substances between mud and water in lakes. J. Ecol. **30:** 280–329.

OUELLETTE, D., G. DESROSIERS, J. P. GAGNE, F. GILBERT, J. C. POGGIALE, P. U. BLIER, AND G. STORA. 2004. Effects of temperature on in vitro sediment reworking processes by a gallery biodiffusor, the polychaete *Neanthes virens*. Mar. Ecol. Prog. Ser. **266:** 185–193, doi:10.3354/meps266185

R DEVELOPMENT CORE TEAM. 2006. R: A language and environment for statistical computing. R Foundation for Statistical Computing.

REISE, K. 1983. Biotic enrichment of intertidal sediments by experimental aggregates of the deposit-feeding bivalve *Macoma balthica*. Mar. Ecol. Prog. Ser. **12:** 229–236, doi:10.3354/meps012229

SAVCHUK, O. P., F. WULFF, S. HILLE, C. HUMBORG, AND F. POLLEHNE. 2008. The Baltic Sea a century ago—a reconstruction from model simulations, verified by observations. J. Mar. Syst. **74:** 485–494, doi:10.1016/j.jmarsys.2008.03.008

SLOMP, C. P., E. H. G. EPPING, W. HELDER, AND W. VAN RAAPHORST. 1996. A key role for iron-bound phosphorus in authigenic apatite formation in North Atlantic continental platform sediments. J. Mar. Res. **54:** 1179–1205, doi:10.1357/0022240963213745

———, J. THOMSON, AND G. J. DE LANGE. 2002. Enhanced regeneration of phosphorus during formation of the most recent eastern Mediterranean sapropel (S1). Geochim. Cosmochim. Acta **66:** 1171–1184, doi:10.1016/S0016-7037(01)00848-1

SMITH, C. R., L. A. LEVIN, D. J. HOOVER, G. MCMURTY, AND J. D. GAGE. 2000. Variations in bioturbation across the oxygen minimum zone in the northwest Arabian Sea. Deep-Sea Res. Part II. **47:** 227–257, doi:10.1016/S0967-0645(99)00108-3

SOETAERT, K., AND P. M. J. HERMAN. 2009. A practical guide to ecological modelling: Using R as a simulation platform. Springer.

———, ———, AND J. J. MIDDELBURG. 1996. A model of early diagenetic processes from the shelf to abyssal depths. Geochim. Cosmochim. Acta **60:** 1019–1040, doi:10.1016/0016-7037(96)00013-0

———, AND J. J. MIDDELBURG. 2009. Modeling eutrophication and oligotrophication of shallow-water marine systems: The importance of sediments under stratified and well-mixed conditions. Hydrobiologia **629:** 239–254, doi:10.1007/s10750-009-9777-x

———, T. PETZOLDT, AND R. W. SETZER. 2010. Solving differential equations in R: Package deSolve. J. Stat. Softw. **33:** 1–25.

STIGEBRANDT, A. 1991. Computations of oxygen fluxes through the sea surface and the net production of organic matter with application to the Baltic and adjacent seas. Limnol. Oceanogr. **36:** 444–454, doi:10.4319/lo.1991.36.3.0444

TROMP, T. K., P. VAN CAPPELLEN, AND R. M. KEY. 1995. A global model for the early diagenesis of organic carbon and organic phosphorus in marine sediments. Geochim. Cosmochim. Acta **59:** 1259–1284, doi:10.1016/0016-7037(95)00042-X

TURNER, R. E., N. N. RABALAIS, AND D. JUSTIC. 2008. Gulf of Mexico hypoxia: Alternate states and a legacy. Environ. Sci. Technol. **42:** 2323–2327, doi:10.1021/es071617k

VAHTERA, E., AND OTHERS. 2007. Internal ecosystem feedbacks enhance nitrogen-fixing cyanobacteria blooms and complicate management in the Baltic Sea. Ambio **36:** 186–194, doi:10.1579/0044-7447(2007)36[186:IEFENC]2.0.CO;2

VAN CAPPELLEN, P., AND Y. WANG. 1995. Metal cycling in surface sediments: Modeling the interplay of transport and reaction, p. 1–10. *In* H. E. Allen [ed.], Metal contaminated sediments. Ann Arbor Press.

WANG, Y., AND P. VAN CAPPELLEN. 1996. A multicomponent reactive transport model of early diagenesis: Application to redox cycling in coastal marine sediments. Geochim. Cosmochim. Acta **60:** 2993–3014, doi:10.1016/0016-7037(96)00140-8

WASMUND, N., AND OTHERS. 2001. Trophic status of the south-eastern Baltic Sea: A comparison of coastal and open areas. Estuar. Coast. Shelf Sci. **53:** 849–864, doi:10.1006/ecss.2001.0828

WESTRICH, J. T., AND R. A. BERNER. 1984. The role of sedimentary organic matter in bacterial sulphate reduction: The G model tested. Limnol. Oceanogr. **29:** 236–249, doi:10.4319/lo.1984.29.2.0236

ZETTLER, M. L., M. RÖHNER, AND J. FRANKOWSKI. 2006. Long term changes of macrozoobenthos in the Arkona Basin (Baltic Sea). Boreal Environ. Res. **11:** 247–260.

Associate editor: Bo Thamdrup

Received: 21 July 2010
Accepted: 31 January 2011
Amended: 24 February 2011